

Yield precursor dislocation avalanches in small crystals: the irreversibility transition

Xiaoyue Ni^{1*}, Haolu Zhang¹, Danilo B. Liarte², Louis W. McFaul³, Karin A. Dahmen³, James P. Sethna², and Julia R. Greer¹

¹*Division of Engineering and Applied Sciences, California Institute of Technology, Pasadena, CA 91125*

²*Laboratory of Atomic and Solid State Physics, Cornell University, Ithaca, New York 14853-2501*

³*Physics Department, University of Illinois at Urbana-Champaign, Urbana, IL 61801*

TABLE OF CONTENTS

S1.	Experimental method	1
S2.	Reconstruction of reloading stress-strain	5
S3.	Precursor avalanches in different size pillars under different loading modes	10
S4.	Drift and elastic strain correction in the training experiment	12
S5.	Weighted fit and significance	14
S6.	Theoretical prediction for the power-law exponent.....	16
S7.	Justification of critical stress and transition behavior	17
S8.	Effect of stress rate on precursor dissipation	19
S9.	Precursor dissipation training for different pillar sizes	20
	References	22

S1. EXPERIMENTAL METHOD

We use single-crystalline Cu nano- and micro-pillars as our study system. We fabricate the cylindrical samples from a bulk single-crystalline copper (purchased from MTI Corporation) that is of purity > 99.9999% and with top surface polished to $a < 30 \text{ \AA}$ RMS roughness, following a concentric-circles top-down methodology using a Focused Ion Beam (FIB). We use 30 kV gallium ion beam starting with an ion current of 5 nA for outer-ring milling and reduce the current in steps to 30 pA for the finish up in order to suppress gallium ion implantation as well as sidewall tapering. The pillar diameters range from 300 nm to 3 μm . The nominal aspect ratio (height/diameter) is 3:1. Although FIB introduces surface damage to the pillars, the Ga⁺ ion implantation depth is limited, on the order of 5-10 nm, and usually manifests as dead dislocation loops or a thin amorphous layer and likely contribute negligibly to the overall mechanical

* To whom all correspondences should be addressed. Email: xni@northwestern.edu

response. The mechanical properties of the exact 500 nm pillar arrays tested have been reported in Ref. [1]. The sample is oriented in the $\sim \langle 111 \rangle$ loading direction.

We carry the nanomechanical experiments in a nanoindenter (Triboindenter, Hysitron) equipped with a custom made 8 μm -diameter diamond flat punch. All performed tests are uniaxial compression tests that fall in one of the three categories: (1) displacement-controlled (DC) monotonic-loading, (2) load-controlled (LC) monotonic-loading, and (3) load-controlled (LC) cyclic-loading tests. In a monotonic test, the pillar is compressed to a target load/displacement and then fully unloaded. A cyclic test consists of multiple subsequent unload-reload tests. Note there are two types of cyclic tests: (i) gradually-increasing maximum stress *unload-reload* test designed to compare the in-general precursor avalanche behavior between large and small size pillars, and (ii) the constant-maximum-stress-in-one-step but increasing-stress-between-steps *training* test for the purpose of characterizing RIT behavior.

Both load and displacement control are implemented via standard PID feedback loop. The sampling rate of the controller is 78 kHz. The physical input-output response involves a time lag that depends on the sample as well as the designed PID control gain parameters. In our experiments, we set proportional gain $P = 0$, integral gain $I = 1$, and derivative gain $D = 0$ for LC tests, whereas $P = 0$, $I = 0.6$, $D = 0$ for DC tests.

An example of the system's response to a step displacement function in air using the same control parameters as in our tests is shown in Fig. S1, where the system response time is found to be ~ 14 ms.

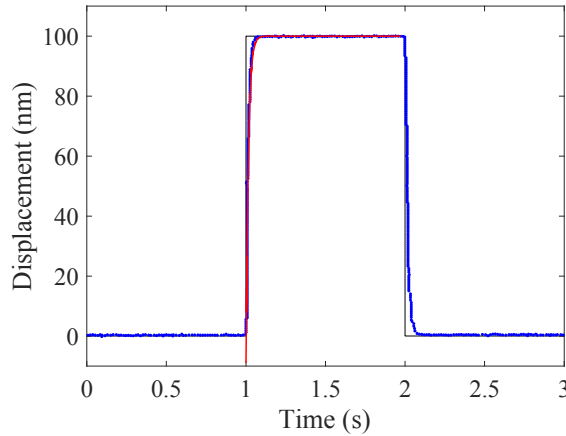


Fig. S1. **System response to a prescribed step function in air.** The displacement is controlled with control parameters $P=0$, $I=0.6$, $D=0$. The data (blue) is fitted to a standard exponential function (red) to find the characteristic response time.

During a fast avalanche, the pillar stiffness quickly drops to near zero, leaving only the axial machine stiffness ($\sim 10^2$ N/m) in effect at the same load level, which will result in a displacement burst to release the extra stored elastic energy as well as an abrupt drop in load. After the energy

release, in LC tests, the decrease in load is accounted for through sequential reloading, whereas in displacement-controlled tests, the overshoot displacement is unloaded to resume the prescribed displacement.

Maaß *et. al*² did uniaxial compression tests on Au micropillars using the same instrument as used in this study. The work shows that the LC mode lowers the effective machine stiffness to the order of ~ 1 N/m, whereas the DC mode imposes an artificial stiffening to the system and raised the effective machine stiffness to $\sim 10^3$ N/m, resulting in the LC mode producing overall larger dislocation avalanches than the DC mode, which explains the large difference in the plastic avalanche size between DC and LC tests. In our experiment on copper pillars, we measure the LC effective machine stiffness to be ~ 260 N/m while DC stiffness to be ~ 450 N/m.

We report all our experimental results in engineering stress σ_{eng} and strain ε_{eng} , which have simple linear relationships with the raw load P and displacement u measurements:

$$\begin{aligned}\sigma_{eng} &= P/A_0, \\ \varepsilon_{eng} &= u/L_0, \#(S. 1)\end{aligned}$$

where A_0 is the original cross-sectional area and L_0 is the original height of the pillar. Fig. S2(a) shows the displacement-load measurements of a representative training experiment on a 3 μm diameter copper pillar, in comparison to the its linearly-converted engineering stress-strain data shown in Fig. S2(b).

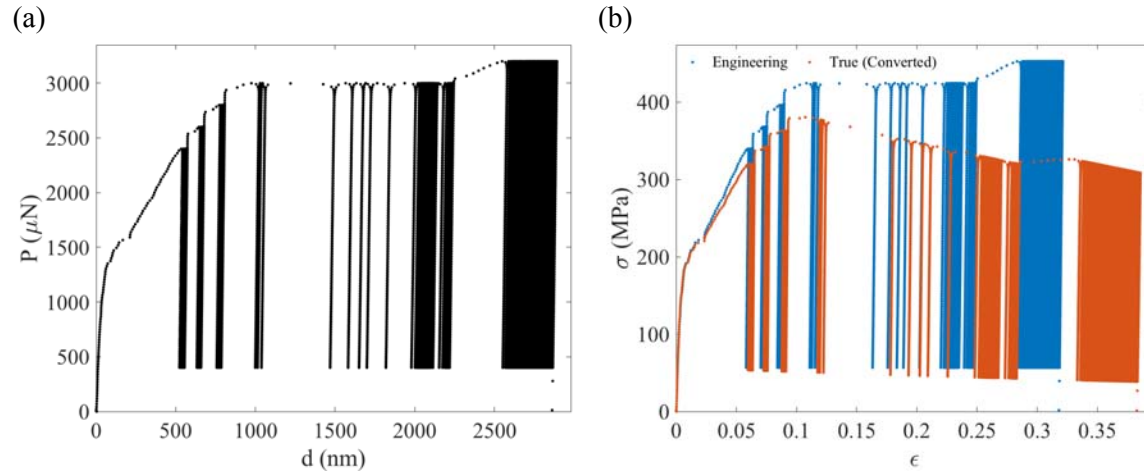


Fig. S2. Representative test measuring (a) the displacement and load data, and (b) the reported engineering stress strain (blue) in comparison to the estimated true stress strain data (red).

In Fig. S2(b), we also present the theoretically estimated true stress σ_{tru} and true strain ε_{tru} with zero-stress state volume conservation assumption (which holds true for uniaxial compression experiments on micropillars loaded in a high-symmetry orientation), *i.e.* under elastic loading the pillar can dilate or contract, but plastic volume must conserve at unloaded state:

$$A_0 L_0 = A_p L_p. \#(S. 2)$$

The subscript p here denotes the unloaded plastically-deformed state of the pillar. When plasticity happens the zero-stressed sample evolves via plastic strain,

$$\varepsilon_p = - \int_{L_0}^{L_p} \frac{dL}{L} = - \ln \frac{L_p}{L_0}. \#(S. 3)$$

The elastic deformation does not change the sample intrinsically. The elastic strain follows Hooke's law in uniaxial loading case,

$$\varepsilon_e = \sigma_{tru}/E, \#(S. 4)$$

where E is the Young's modulus of the sample material. Then the true stress and true strain are calculated as,

$$\begin{aligned} \sigma_{tru} &= \frac{P}{A_p} = \frac{P L_p}{A_0 L_0}, \\ \varepsilon_{tru} = \varepsilon_e + \varepsilon_p &= \frac{P L_p}{E A_0 L_0} - \ln \frac{L_p}{L_0}. \#(S. 5) \end{aligned}$$

In the equations, the only unknown variable, the plastically-deformed length of the pillar L_p , can be estimated from the raw load-displacement measurement:

The instrument measures stiffness k_{meas} as a series combination of pillar stiffness k_{pillar} and Sneddon stiffness³ $k_{sneddon}$,

$$\frac{1}{k_{meas}} = \frac{1}{k_{pillar}} + \frac{1}{k_{sneddon}}. \#(S. 6)$$

The Sneddon stiffness considers the compliance associated with the pillar acting like a flat punch indenting into the bulk substrate,

$$k_{sneddon} = \frac{2E_{substrate}\sqrt{A_c}}{\sqrt{\pi}(1-\nu^2)}, \#(S. 7)$$

where $E_{substrate} = E$ is the Young's modulus of the copper substrate, A_c is the contact area between the pillar and the substrate, and ν is the Poisson's ratio of the pillar material. The total measured displacement is,

$$\begin{aligned} u &= u_p + u_e + u_{sneddon} \\ &= (L_0 - L_p) + \frac{P L_p^2}{E A_0 L_0} + \frac{P \sqrt{\pi}(1-\nu^2)}{2E \sqrt{A_c}}. \#(S. 8) \end{aligned}$$

For simple analytical solution, we assume that A_c remains constant during deformation. The initial contact area can be estimated from the measured tapering angle θ of typical FIB-machined copper pillars, $A_c = \pi(L_0 \tan\theta + \sqrt{A_0/\pi})^2$.

We use experimentally measured modulus of the copper sample in the equation and solve for L_p ,

$$L_p = \frac{EA_0L_0}{2P} \left(1 - \sqrt{1 - \frac{4P}{EA_0L_0} \left(L_0 - u + \frac{P\sqrt{\pi}(1-\nu^2)}{2E\sqrt{A_c}} \right)} \right). \#(S.9)$$

We substitute L_p to Eq. (S.5) to obtain the true stress-strain estimation. Table S1 below shows the sample geometry and material parameters we use in the conversion for 3 μm diameter copper pillars.

Table S1: Sample Parameters

Initial Cross-Sectional Area	$A_0 =$	7 μm^2
Initial Length	$L_0 =$	9 μm
Young's Modulus	$E =$	140 GPa
Poisson Ratio	$\nu =$	0.33
Tapering Angle	$\theta =$	4°

As shown in Fig. S2 (b), as the true cross-sectional area A_p increases with greater plastic strain, the true applied stress decreases while plastic deformation occurs at a constant load. As the true stress-strain conversion holds only in the conditions that (i) the lattice orientation does not change significantly and (ii) deformation remains approximately homogeneous on the pillar scale, the post-failure true stress-strain estimation is not reliable.

S2. RECONSTRUCTION OF RELOADING STRESS-STRAIN

In this paper, we apply a reloading stress-strain reconstruction protocol to analyze the yield-precursor behavior for different sizes of pillars. Fig. S3(a) shows a sample stress-strain data of load-controlled (LC) uniaxial compression tests on a 500 nm diameter pillar with prescribed unload-reload cycles. The cyclic loading rate is ~ 400 MPa/s, while the maximum stress is increased by ~ 5 MPa per cycle, which is equivalent to a quasistatic ramping rate of ~ 1.4 MPa/s. We keep the minimum stress at ~ 40 MPa to maintain tip-sample contact. As the occurrence of avalanches upon reloading is stochastic in small-scale crystals, the main purpose of the stress-strain reconstruction is to average all the reloading curves as a measure of the ensemble precursor deviation from the textbook “peak stress” yielding.

We first shift the origin of each reloading process such that the stress is zeroed at the previous maximum stress (usually at the start of unloading) and the strain is zeroed at the beginning of each reloading, which is demonstrated in Fig. S3(b). During reloading, if a new avalanche happens before reaching the previous maximum stress (re-zeroing stress), it is a precursor avalanche.

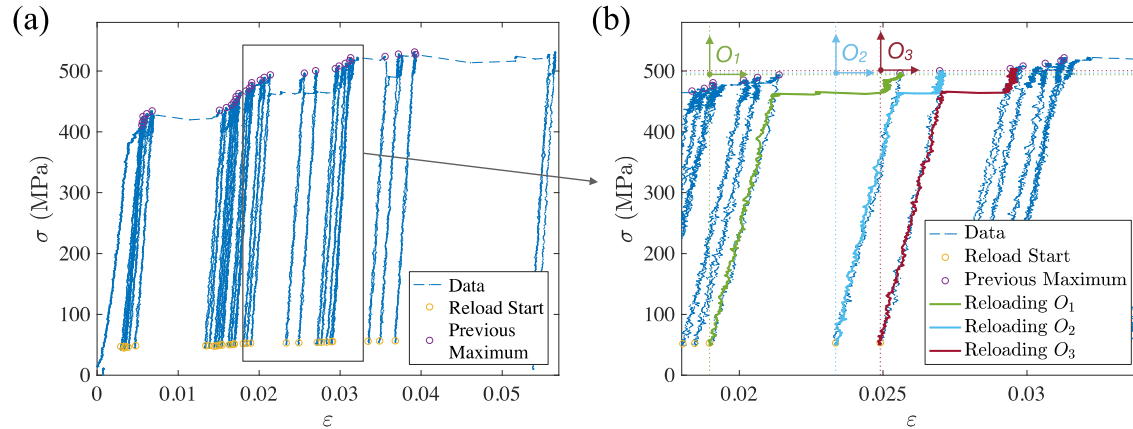


FIG. S3. **Re-zeroing reloading stress-strain in unload-reload experiments:** (a) A sample stress-strain curve for the unload-reload test on a 500 nm diameter Cu pillar, marked with the start of each reloading (yellow circle) and the point at which the previous maximum stress occurs (purple circle) (b) A closer look at the sample unload-reload cycles, where the stress of each reloading is re-zeroed with the previous maximum stress (textbook yield stress updated upon deformation) and the strain is re-zeroed with the starting strain of the reloading process. The shifted stress-strain origin is labeled as O_1 for the first marked reloading process (light green), O_2 for the second (light blue), O_3 for the third (dark red), and so on.

Each re-zeroed reloading process for any pillar is then treated as an individual reloading test on one nanopillar. The total precursor behavior for the pillars can be reconstructed according to a Gedanken experiment on a macroscopic sample composed of stacks of nanopillars either in parallel or in series, as illustrated in Fig. S4(a). We interpolate and average the reloading response of each pillar along the monotonically increasing strain ϵ_0 (in-parallel) or stress σ_0 (in-series) for the ensemble response. Fig. S4(b) shows examples of the in-series and in-parallel interpolation of the single reloading curve shown in Fig. S3(b) and zeroed at O_1 .

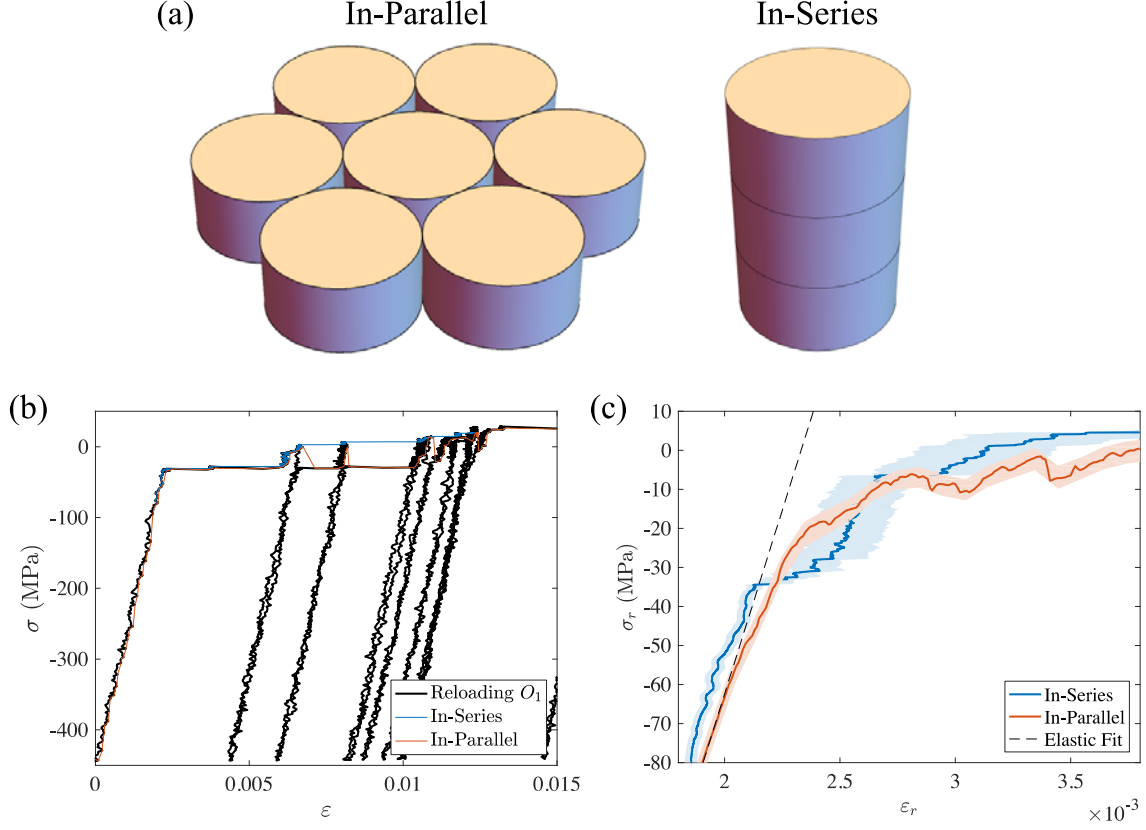


FIG. S4. **Stress-strain reconstruction according to the Gedanken compression experiments on micropillars** (a) Schematics of the Gedanken compression experiments with prescribed strain (in-parallel) and prescribed stress (in-series) configurations. (b) Examples of the in-series strain and in-parallel stress interpolation of the single reloading curve shown in Fig. S3(b) and zeroed at origin O_1 . (c) The averaging stress-strain reconstruction of the reloading curves for both in-parallel and in-series cases for the sample load-controlled (LC) test shown in Fig. S3.

In the in-parallel configuration, for the i^{th} pillar, strain $\epsilon_i = \epsilon_0$ is controlled and stress σ_i encodes the material's response. The system composed of N pillars has a stress response,

$$\begin{aligned}
 \sigma_r &= \frac{1}{N} \sum_{i=1}^N \sigma_i \\
 &= \frac{1}{N} \sum_{i=1}^N (E_i + \delta E_i) \epsilon_0 \\
 &= E \epsilon_0 + \frac{1}{N} \sum_{i=1}^N \delta E_i \epsilon_0 \\
 &= (E + \delta E) \epsilon_0. \#(S. 10)
 \end{aligned}$$

In Eq. (S.1), $\delta E = \frac{1}{N} \sum_{i=1}^N \delta E_i$ characterizes the plastic response of the N-pillar system. σ_r and ε_0 are the reconstructed stress and strain. Similarly, the series reconstructed strain ε_r can be expressed with respect to the prescribed stress σ_0 ,

$$\varepsilon_r = (E + \delta E)^{-1} \varepsilon_0. \#(S. 11)$$

Fig. S4(c) shows the sample in-series and in-parallel averaging reconstruction of reloading stress and strain for the same unload-reload test on a 500 nm diameter Cu pillar as shown in Fig. S3. In the main text, we present the in-parallel reconstruction for tests on seven identically-prepared pillars for each size. We keep only the Non-Hookean part of strain in the final results by subtracting the elastic strain fitted from the linear reloading regime, $\sigma_r \in [-300, -100]$ MPa. The elastic fit for the sample in-parallel reconstruction stress-strain is shown in Fig. S4(c).

The same reconstruction analysis can be applied to the conventional quasi-static load- or displacement-controlled nanomechanical experiments. In the monotonic, uniaxial loading experiments, the plastic strain bursts usually lead to drops in the applied force caused by the finite machine stiffness under either displacement or load control (See Sec. S1 for details). Fig. S5(a) shows a sample stress-strain of a load-controlled compression test on a 500 nm diameter Cu pillar, marked with the onset and finish of each avalanche event: at the beginning of a displacement burst of size Δx , the force applied to the sample drops by $k\Delta x$, with k being the machine stiffness. Driven by the feedback control, the indenter tip will re-attain the prescribed load on the sample after a fast avalanche event is completed. This stress-drop-and-catch-up process is manifested as a spontaneous unload-reload response. The stress that initiates an avalanche can be regarded as the updated yield stress of the deformed pillar. The yielding avalanche triggers the following unloading process. When the avalanche finishes, the load control re-engages and starts the reloading process.

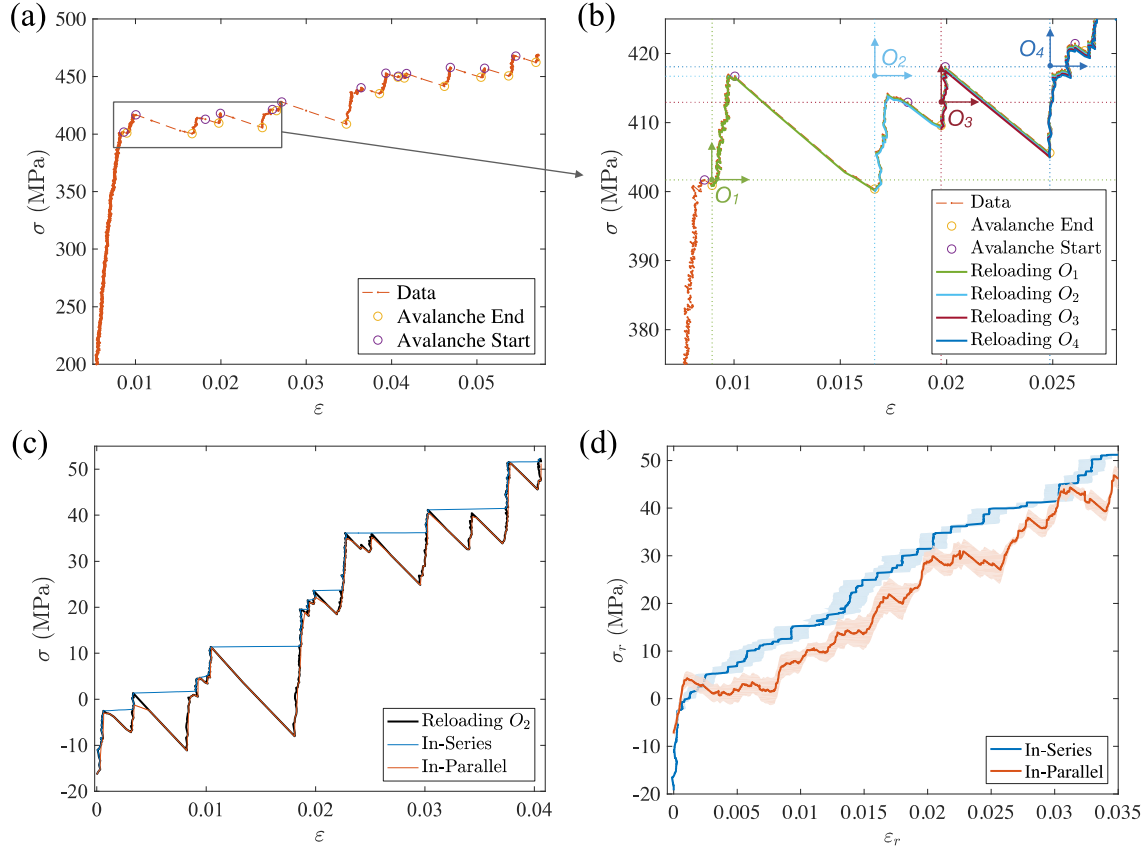


FIG. S5. Stress-strain reconstruction for finding precursor avalanches in the quasi-static load-controlled experiment: (a) A sample stress-strain curve for the load-controlled test on a 500 nm diameter Cu pillar, marked with the onset and finish of each avalanche event. (b) A closer look at the avalanches, where the stress after each avalanche is re-zeroed with the previous maximum stress (textbook new yield stress) and the strain is re-zeroed with the starting strain of the reloading process. The re-zeroed stress-strain origin is marked as O_1 for the first seen avalanche, O_2 for the second, and so on. (c) Examples of in-series strain and in-parallel stress interpolation of the single reloading curve shown in (b), zeroed at origin O_1 . (d) The averaging in-parallel and in-series stress-strain reconstruction of all reloading curves shown in (a).

Fig. S5(b-d) exemplify the reconstruction process for the load-controlled experiment shown in Fig. S5(a) following the same protocol as the one applied to the unload-reload experiments: we (b) shift origins of the stress-strain data after each yielding avalanche with the stress zeroed at the start of the avalanche and strain zeroed at the end of the avalanche, (c) interpolate the in-series strain or in-parallel stress, and (d) take averages of the interpolated strain/stress for the stress-strain reconstruction.

S3. PRECURSOR AVALANCHES IN DIFFERENT SIZE PILLARS UNDER DIFFERENT LOADING MODES

We performed the stress-strain reconstruction analysis for displacement-controlled and load-controlled quasistatic compression tests, as well as unload-reload cyclic compression tests, on different size Cu pillars with diameters of 300 nm, 500 nm, 700 nm, 1 μm , and 3 μm . The sample stress-strain measurements are shown in Fig. S6(a-c), while the in-parallel reconstructed reloading curves are correspondingly shown in Fig. S6(d-f). Each reconstruction analysis takes averages of all reloading curves from individual tests on seven identically-prepared pillars. We have subtracted the elastic strain from the reconstructed strain, leaving only the plastic precursor strain. The reconstructed non-Hookean reloading stress-strain quantitatively evaluates the averaging yield-precursor avalanche behavior of a specific size of Cu pillar under a specific loading mode.

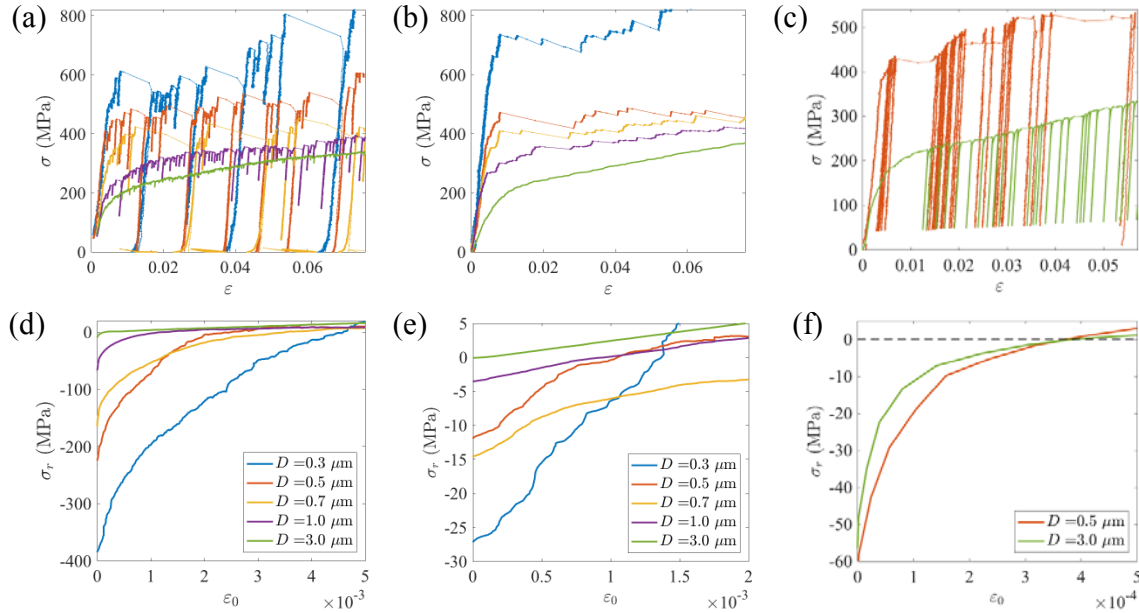


FIG. S6. **Precursor avalanches present in different loading-mode uniaxial compression experiments on different size Cu pillars.** Sample stress-strain (top) and in-parallel reconstructed non-Hookean stress-strain (bottom) for (a, d) displacement-controlled (DC) monotonic-loading, (b, e) load-controlled (LC) monotonic-loading, and (c, f) unload-reload cyclic-loading compression experiments on different size pillars. In general, less precursor dissipation is observed in larger Cu pillars.

In all cases, precursor dissipation is prevalently observed in small pillars. We can gain some insights into the precursor avalanche behavior from a comparison amongst the different loading mode results. 1. Larger precursor strains are observed in displacement-controlled tests than load-controlled tests. As shown in Fig. S6(a) and (b), the avalanche-induced unloading amplitudes in displacement-controlled tests are on average larger than those in the load-controlled experiments. This might infer that the size of precursor strains is dependent on unloading stress amplitude. 2.

The precursor strains in unload-reload tests are much smaller than those of the displacement-controlled tests, though the unloading amplitude is of the similar scale (for the 500 nm diameter pillars). One possible explanation is that part of the “precursor strains” observed in the quasistatic compression tests are “unfinished” avalanches caused by non-perfect control: unlike the prescribed unloading in unload-reload tests, unloading processes in the monotonic loading test are spontaneously triggered by fast avalanches; thus, stress always drops during a slip event, which might interrupt the growing avalanche, leaving residual avalanche to be re-activated upon the subsequent reloading process. 3. Larger precursor dissipations are observed in smaller pillars. This emergent size dependency can be an intrinsic size effect of materials’ yield precursor behavior; on the other hand, it can also be a result of smaller pillars undergoing larger unloading amplitude as shown in Fig. S6 (a) and (b) – smaller pillars exhibit larger strain bursts, which in turn, will give larger stress drops due to the inherent machine stiffness in both displacement- and load-controlled tests.

To the best of the authors’ knowledge, phenomena similar to the presented yield-precursor avalanche hysteresis has not been explicitly resolved in the conventional macroscopic mechanical tests nor in the uniaxial micro- or nanopillar compression experiments. Based on the unloading-reloading experiment results (Fig. S6(f), same as Fig. 1d in the main text), the precursor avalanches observed in the submicron-size samples (for example, an average ensemble precursor strain of $\sim 10^{-4}$ that occurs at $\sim 5\%$ (20 MPa) below the measured yield stress (400 MPa) in 500 nm diameter pillars) are expected to be detectable in bulk experiments⁴ where the entire elastic strain at the yield stress is ordinarily $< 10^{-2}$. To systematically study the size effect, we need to do the same experiments on significantly larger size pillars, which reaches the limit of our nanomechanical experiment capability: The instrument has a load limit of 10 mN and a displacement limit of 5 μm . While the critical failure of 3 μm pillar happens at a load of ~ 3 mN and a displacement of ~ 1 μm , we can only reasonably increase the system size by a factor of ~ 2 .

Note that the reduction in the precursor avalanche hysteresis for larger system sizes is not related to the difficulties in measuring dislocation avalanches in macroscopic fcc materials (as opposed to lower symmetry hexagonal materials like zinc and ice¹²). We measure the avalanche-induced hysteresis – the sum of the effects of avalanches that may (for large pillars) be individually beyond our instrumental resolution.

The current observation that larger samples give smaller precursor avalanches is similar to the system size effect on plastic avalanches, which has been revealed also in micropillar compression experiments⁵. Former studies have attributed the finite-size effect on plastic avalanche size to single-arm source mechanism^{6,7} surface source nucleation and dislocation annihilation^{8,9}, and thin film plasticity^{10,11}. Similar statements could be made for the precursor

avalanches at the small-scale, but with the current available data, we cannot distinguish between these different speculations.

We have also applied our analysis to simulated data (using 3D discrete dislocation dynamics) and observed similar qualitative behavior (G. Costantini and S. Zapperi, unpublished). Further investigation on the emergent size effect, e.g. doing same-amplitude unload-reload tests on different sizes of pillars, is beyond the scope of this work.

S4. DRIFT AND ELASTIC STRAIN CORRECTION IN THE TRAINING EXPERIMENT

We study how the precursor behavior changes over deformation using the training experiment, where we repeat loading to the same maximum stress and increase the maximum stress in steps. We evaluate the energy dissipated by precursor avalanches from an integral over each unload-reload hysteresis cycle, $U = \int \sigma d\varepsilon$. During tests with long unloading/reloading segment time, the instrumental drift in the machine can result in large discrepancies between the measured displacement and the actual sample displacement. This can give rise to errors in the calculation of the precursor hysteresis, which is very sensitive to the measurement of displacement during each unload-reload cycle. Fig. S7(a) and (b) demonstrate the drift problem in the training experiment on 3 μm diameter Cu pillars by comparing the precursor hysteresis calculated over cycles of the same maximum stress ~ 350 MPa between the tests with 2 s (short), 80 MPa amplitude unloading/reloading segments and the tests with 4 s (long), 160 MPa amplitude unloading/reloading segments. Both tests use the same loading rate of 40 MPa/s. For the 4 s segment tests shown in Fig. S7(b), the precursor dissipation decays to negative values, which is unphysical for a uniaxial compression test on single crystalline metals. The negative hysteresis that is slowly-varying over time can be explained by the usually negative thermal drift present in the nanoindentation tests. We apply drift correction to each unload-reload cycle. Fig. S7(c) shows the post-drift-correction precursor hysteresis vs. cycle data for the same set of 4 s segment tests, which mitigates the unphysical negative values and exhibits similar decay-over-cycle behavior as that for the short segment test.

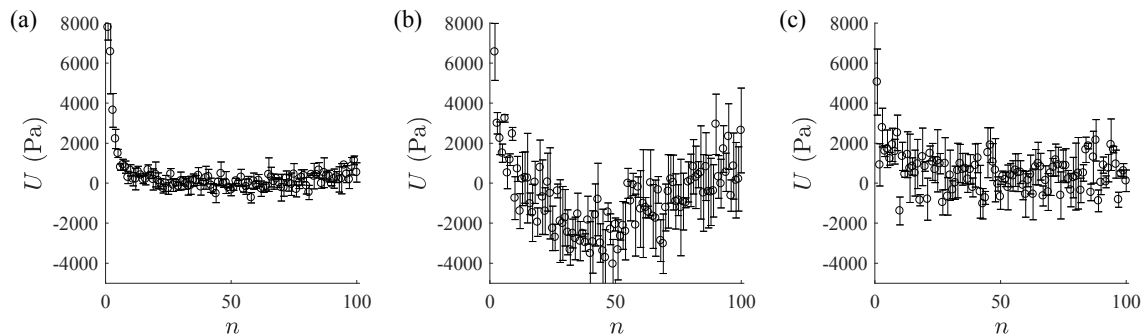


FIG. S7. **Effect of instrumental drift on the calculated precursor dissipation for 3 μm diameter Cu pillars.** (a) Tests with 2 s (short) individual unloading/reloading segments show a clean decay of the

average precursor dissipation. (b) Average precursor dissipation for tests with 4 s (long) unloading/reloading segments exhibit unphysical negative values, which indicates a potential error in the strain measurements due to instrumental drift. (c) A drift correction on the 4 s segment test data mitigates the negative values and discloses a decay behavior.

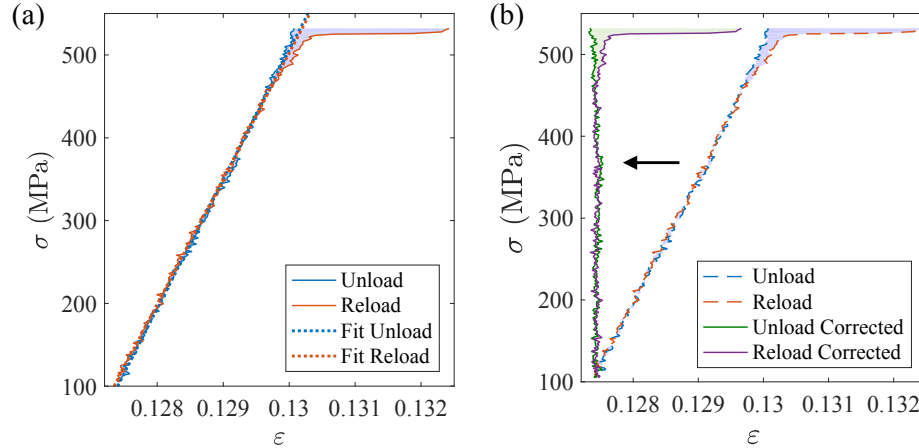


FIG. S8. **Demonstration of the drift correction process:** (a) An example raw stress vs. strain data of subsequent unloading and reloading segments (of a 1 μm diameter copper pillar). The segments are individually linearly fitted to account for the slow instrumental drift in addition to the Hookean elastic strain; The fitting excludes data in the top 80 MPa segment within which precursor avalanches are present. (b) The linearly fitted strains are subtracted from the unloading and reloading segments respectively to correct for the instrumental drift. The shaded area in the figures indicates the precursor hysteresis calculated from its corresponding set of data.

The drift correction is applied to each unload-reload cycle as the following. We take one raw stress-strain cycle shown in Fig. S8(a) as an example. The precursor hysteresis associated to the cycle is marked by the shaded area. Since the individual unloading/reloading segment duration ($< 1\text{s}$) is short, the drift rate during each segment is assumed to be constant. A linear fit is prescribed to each unloading/reloading segment below the onset stress of precursor avalanches (the top 80 MPa segment), to account for the Hookean strain as well as the linear drift. In Fig. S8(b), we subtract the linearly fitted strain from the overall unloading/reloading strain for the drift-corrected hysteresis behavior. The post-correction deformation is plastic only.

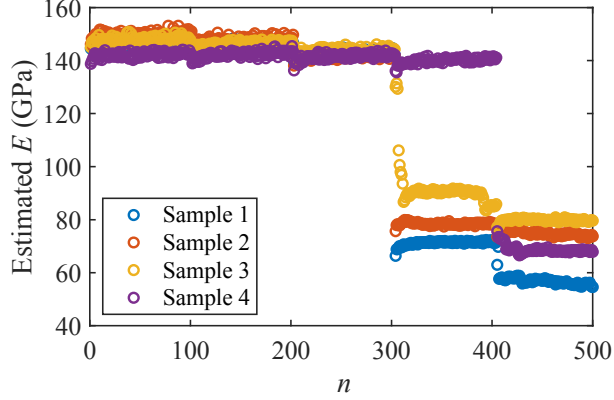


FIG. S9. **Tangent modulus estimate vs. cycle.** The tangent modulus stays almost constant at around ~ 140 GPa before loading reaches σ_c .

The linear fit is a combination of modulus and instantaneous drift. When the instrumental drift and the change in pillar geometry is small, the fitting results should not deviate much from the nominal Young's modulus for copper. Fig. S9 shows the tangent estimated modulus vs. cycle analysis for four sample training tests. Before the catastrophic failure occurs, where our true stress-strain conversion holds in the conditions that (i) the lattice orientation does not change significantly and (ii) deformation remains approximately homogeneous on the pillar scale, the tangent modulus estimate stays constant at around ~ 140 GPa and agrees well with the nominal Young's modulus of copper.

S5. WEIGHTED FIT AND SIGNIFICANCE

Each training experiment is prescribed with five 100 cyclic loading steps with maximum stress σ_{max} that fall in the range of 228 – 452 MPa. We extend the cycle number at step 452 MPa to 500 for a more sufficient decay around the critical stress – we prescribe long cycles only at the last step of the training test due to concerns for instrumental drift. We apply the multistep cyclic load function to twenty-four identically prepared $3 \mu\text{m}$ -diameter copper samples. Among the 24 pillars, 13 were tested at maximum stresses from 228 to 452 MPa with an interval of 56 MPa, 7 were tested from 340 to 452 MPa with an interval of 28 MPa, and 4 were tested at 172, 200, 228, 340, and 452 MPa. We normalize σ_{max} by the flow stress of each experiment, and then binned it for the training behavior analysis. The binning average σ_{max} spans the stress range $0.5 - 1.0 \sigma_c$. It is reasonable to assume that for the n^{th} cycle at a specific σ_{max} , the intrinsic precursor dissipation behavior $U(n)$ is equivalent across all samples within statistical variation. We therefore report $U(n)$ in stress-binning mean and standard error.

We characterize the decay behavior $U(n)$ at each σ_{max} using a fitting function $U_f(n)^{13}$,

$$U_f(n) = (U_0 - U_\infty)e^{-n/\tau}n^{-\delta} + U_\infty, \quad (\text{S.12})$$

where we evaluate the steady-state value U_∞ as the average of the last N_0 cycles[†] in which range U settles to a plateau, and fit for U_0 and τ . We presume $N_0 = 100 - 3\tau_0$, ($N_0 \geq 1$) using the empirical scaling¹³, $\tau_0 = 3(1 - \sigma)^{-1.1}$. δ is evaluated from a simple power law fitting to the approximate critical behavior at $\sigma_{max} \sim \sigma_c$,

$$U_f'(n) = U_f(n; \tau \rightarrow \infty, U_\infty \rightarrow 0) = U_0 n^{-\delta}. \quad (\text{S.13})$$

We use the 500 cycle training data at stress step $\sigma_{max} \sim \sigma_c$ for the power-law fitting for δ , as shown in Fig. S10. Over large number of cycles with the engineering maximum stress prescribed to be constant, the large plastic deformation in high-symmetry direction can cause a decrease in the true maximum stress applied to the sample due to volume conservation. As the cycling at the stress level above the critical stress goes, the maximum stress eventually falls below the critical stress over large precursor strain – the precursor dissipation does not decay to finite steady-state value over long cycling tests. The approximate power-law fitting gives $\delta = 0.68 \pm 0.02$.

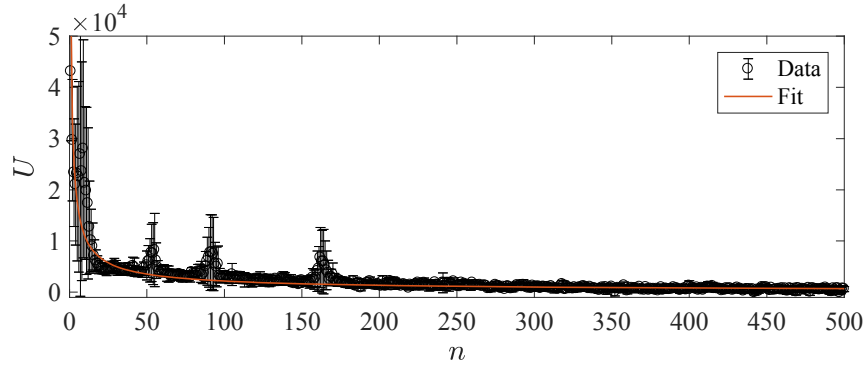


FIG. S10. **Power-law fitting to the long cycling training behavior.** The precursor dissipation vs. cycle behavior at the stress $\sigma_{max} \sim \sigma_c$ is approximately critical and can be characterized by a simple power-law decay for the fitting of the power-law exponent δ in the general model. The mean value spikes at $n \sim 55, 92, 162$ are occasional large precursor avalanches present in individual tests.

For a crosscheck, we use the general model Eq. (S.12) but release δ as a third fitting parameter in addition to U_0 and τ . The fitting results shown in Fig. S11 verify a relatively constant δ for all stress steps, of which the average is 0.7 and agrees with the power-law fitting value. We report the standard deviation of the collective fit as a δ -fluctuation estimation. The fitted values for τ using this method does not give much information due to the large error bars related to releasing a third degree of freedom in the fitting process.

[†] In the all-steps, truncated power-law fitting analysis, we use only the first 100-cycle data of the 500-cycle step.

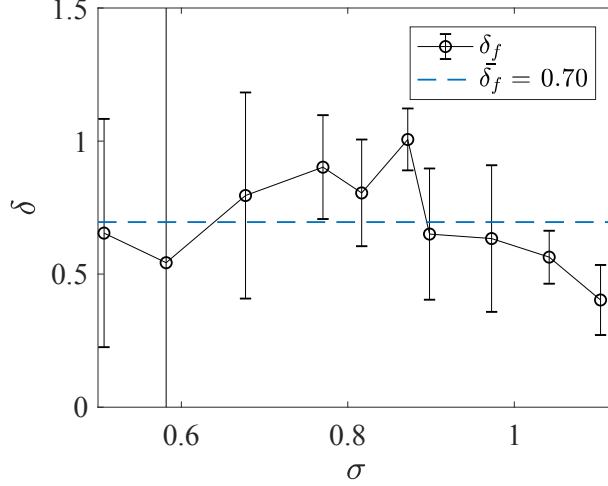


FIG. S11. **Fitting for the power-law exponent.** The fitted exponents are relatively constant for all stress steps and average to agree with the power-law fitted exponent $\delta \sim 0.7$.

We apply the fitted mean power-law exponent $\delta = 0.70$ back to the general fitting model Eq. (S.12) for all stress steps. U_0 is the initial value of U_f . The fitting parameters, τ and U_0 , as well as their confidence intervals were obtained using a nonlinear regression model featuring the Levenberg-Marquardt nonlinear least squares algorithm^{14,15}. Each data point is weighted by the measurement error. The estimation error for the k-th parameter is taken as the 95% confidence interval, $2\sigma_k$.

S6. THEORETICAL PREDICTION FOR THE POWER-LAW EXPONENT

Bandi et al.¹⁶ proposed a model for the history dependence of cyclic training in a uniaxially-compressed granular system, which we can modify to generate a ‘mean-field’ model for the RIT transition. They presume a recurrence relation $X_{n+1} = g(X_n)$ between successive cycles that are loaded to the same maximum pressure, where the variable X_n is defined as the packing volume fraction difference between consecutive cycles. The function $g(x)$ has a fixed point $g(x = 0) = 0$, so assuming analytically, they posit a series expansion:

$$X_{n+1} = g(X_n) = X_n - CX_n^2 + \dots \#(S.14)$$

The solution of this equation for n large is: $X_n = \frac{c^{-1}}{n}$. They propose that the corresponding exponent δ should be universal.

We can generalize this model to exhibit a RIT transition, by noting that analyticity does not require the coefficient of the linear term X_n to be 1. We therefore modify this theoretical model to incorporate the exponential decay rate τ ,

$$X_{n+1} = g(X_n) = AX_n - CX_n^2 + \dots \#(S. 15)$$

The Taylor series of $g(X_n)$ begins with AX_n with $A = e^{-n/\tau} < 1$. Then the RIT happens when A goes to one. This modified model provides a mean-field description of the RIT phenomenon with $\delta = 1$. This critical exponent δ , however, is far outside our statistical errors for the collective fit (Fig. S10), but within the fluctuations for δ fit separately for different σ_{max} (Fig. S11).

S7. JUSTIFICATION OF CRITICAL STRESS AND TRANSITION BEHAVIOR

The critical failure stress during each test, σ_c , is determined as the stress level above which the plastic deformation deviates from the linear hardening behavior. From this critical point the micropillar runs into a short segment of stress plateau, which corresponds to an onset of ‘perfect failure’ – the sample is no longer able to support any additional applied load, and the sample continually deforms plastically at a constant stress.

However, the drop in the true flow stress post ‘perfect failure’ (See Fig. 2a in the main text, or Fig. S2b) is an inevitable characteristic of the load/engineering-stress controlled micropillar compression experiments. Pillar loaded in a high-symmetry $\langle 111 \rangle$ orientation plastically deform via crystallographic slip on six slip systems, which have the highest Schmid factor of 0.27. Sample volume is conserved during plastic deformation. Based on these geometrical considerations, the cross-sectional area of the pillar increases with larger strain while the applied load is monitored by the nanoindenter. This will inevitably lead to a decrease in the true applied maximum stress when plastic deformation happens at a constant load, as shown in Fig. S2(b). Plastic flow at a controlled *engineering* stress is not sustainable for single crystals because the dislocations will glide in the readily available slip planes at a shear stress that corresponds to axial engineering stress above the critical stress, and the true stress σ_{tru} , which is different from engineering stress σ_{eng} through $\sigma_{tru} = \sigma_{eng}(A_0/A_p)$, where A_0 is the original cross-sectional area and A_p is the true cross-sectional area, will eventually fall below the critical stress at a sufficiently large precursor strain, as was already described in Sec. S1 (Fig. S2). An increase in engineering stress is required to compensate for the contact area change to maintain the true applied stress above the critical stress level.

The nominally controlled maximum stress close to or post the critical stress is only an approximation, due to the intrinsic limitation of load-controlled micropillar compression tests that perfect flow is not sustainable as large deformation proceeds. Nevertheless, a transition behavior at $\sim \sigma_c$ is unambiguous. If we force $U_\infty = 0$ for all stress steps, the fitted decay time τ blows up ($\tau > 10^{12}$) around and $\sigma_{max} \sim \sigma_c$, as is shown in Fig. S11. The τ divergence from below the critical stress exhibits RIT behavior robustly.

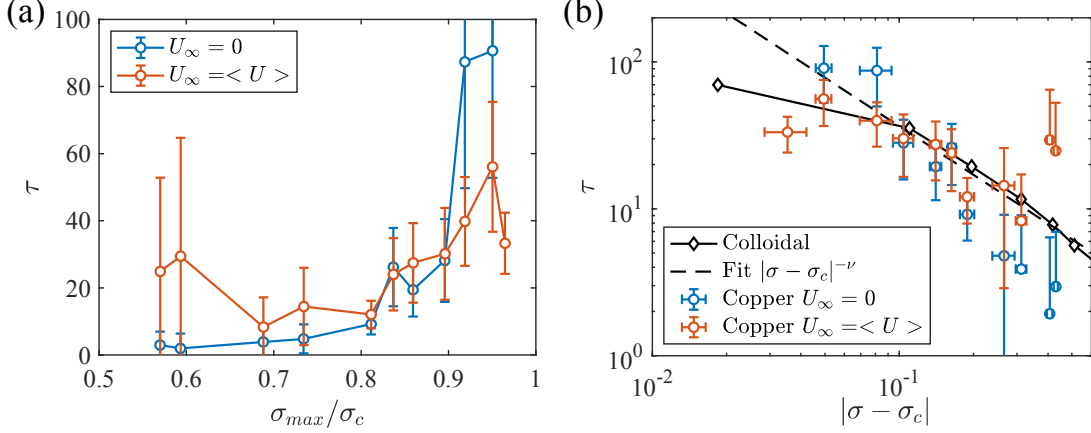


Fig. S12. **The characteristic decay time τ versus maximum stress $\sigma_{\max} = \sigma$ estimated for $3 \mu\text{m}$ diameter pillars with $U_{\infty} = \langle U(n \geq N_0) \rangle$ (Sec. S5) and $U_{\infty} = 0$ cases on (a) a linear scale and (b) a logarithmic scale.**

When the distance from the maximum stress to the critical stress becomes less than 0.1, the fitted decay time constant τ deviates from the RIT scaling,

$$\tau \sim |\sigma - \sigma_c|^{-\alpha}, \#(S.16)$$

where $\alpha = 1.1$ [Ref. 13]. One possible explanation is that when τ becomes large as σ is approaching σ_c , the last N_0 -cycle average estimation for U_{∞} (Sec. S5) is no longer an accurate approximation for a steady state value. When we overestimate U_{∞} , the decay time τ is underestimated, which agrees with what we have observed here.

To prove that the deviation of τ from the theoretical prediction is caused by the limited number of cycles cutting off a sufficient decay for a precise steady state measurement, we apply the same fitting method (Sec. S5) to a simulated $U(n)$ data, where τ is prescribed according to the scaling relation. The simulation generates random $U(n)$ with mean values following Eq. S.12. We extrapolate U_0 from the fit of experimental data and set U_{∞} to be zero. Fig. S13 (a) below shows the simulation data for each theoretical stress step. Fig. S13 (b) and (c) show the fitted τ in comparison with the theoretically prescribed values. The fitted τ deviation shows up in the same way as it does for the experimental data, which means that with only 100 cycle data within one stress step, we do underestimate decay time at stress level close to the critical stress where the theoretical decay constant exceeds 100, using our current fitting method (estimate $U_{\infty} = \langle U(n \geq N_0) \rangle$).

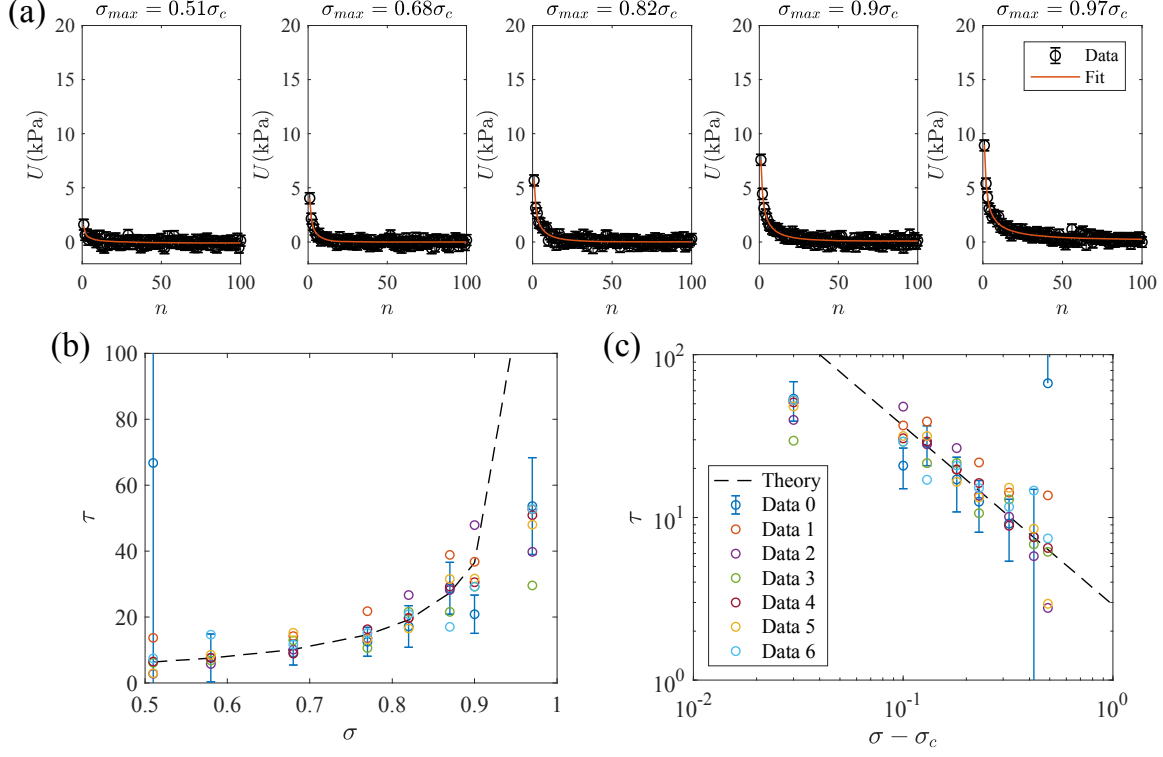


FIG. S13. **Fitting for the decay time constant τ using simulation data with prescribed τ** (a) The simulated data $U(n)$ (*Data 0* in (b) and (c)) at each representative maximum stress σ with τ prescribed according to Eq. (S.16). (b) τ vs. σ estimated for the simulation data, in comparison with the theoretical prescription on a linear scale, and (c) on a logarithm scale, for seven independent simulation runs. We show the representative error bars with one simulation run (*Data 0*). The error bars are statistical fitting errors. The deviation from the theoretical dashed line is the systematic error due to the procedure used to measure the steady-state baseline.

S8. EFFECT OF STRESS RATE ON PRECURSOR DISSIPATION

We apply fast unload-reload cycles with a symmetric loading rate of ~ 570 MPa/s in the training experiment to help reduce the effect of instrumental drift problem. However, this loading rate is too fast to be quasistatic. It is therefore reasonable to suspect that the precursor dissipations could have arisen because of the fast loading mode. To address this issue, we performed small stress amplitude (~ 40 MPa) training tests on $3 \mu\text{m}$ diameter pillars using 3 different stress rates, 40 MPa/s, 290 MPa/s, 570 MPa/s, and calculated the corresponding precursor dissipation over cycles. No drift corrections are applied because of the small stress amplitude which leads to too short linear segment for reliable fitting. The results are shown in Fig. S14 in an increasing stress rate order; it is clear that for the three loading rates the precursor dissipation exhibit a decay behavior over cycles.

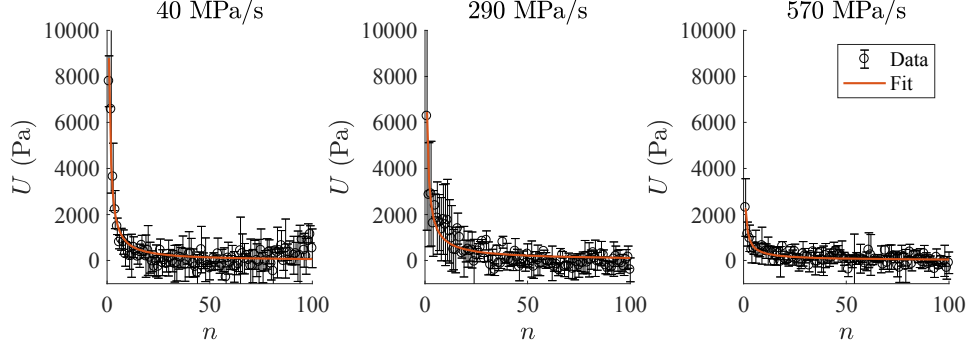


FIG. S14. The precursor dissipation over cycles data and the decay behavior fit for the training experiments with different loading rate of 40 MPa/s, 290MPa/s, and 570 MPa/s.

We characterize the decay behavior using the fitting model $U_f(n; \delta = 0.70)$. The decay time constants for the three tests are estimated to be 6.8 ± 1.8 , 9.8 ± 3.9 , and 7.2 ± 5.9 . This ensures that the precursor avalanches and their self-organizing behavior are not generated by fast loading. On the other hand, the initial precursor dissipation is larger in the slower loading experiments. The emergent stress rate dependency might relate to intrinsic time scales of the small-scale crystal, such as the rate of dislocation relaxation¹.

S9. PRECURSOR DISSIPATION TRAINING FOR DIFFERENT PILLAR SIZES

In addition to 3 μm diameter pillars, we have also performed training tests on 500 nm and 1 μm diameter pillars. For 500 nm diameter pillars, we performed training experiments on a total of twenty-six pillars using six step maximum stress ranging from 550 MPa to 800 MPa with increments of 50 MPa. For 1 μm pillars, we tested seven pillars using five step maximum stress ranging from 300 MPa to 600 MPa with increments of 75 MPa. For both training tests, we unload to a constant minimum stress of 100 MPa (we unload to 56 MPa for 3 μm diameter pillars) to maintain contact between the actuation punch and the sample.

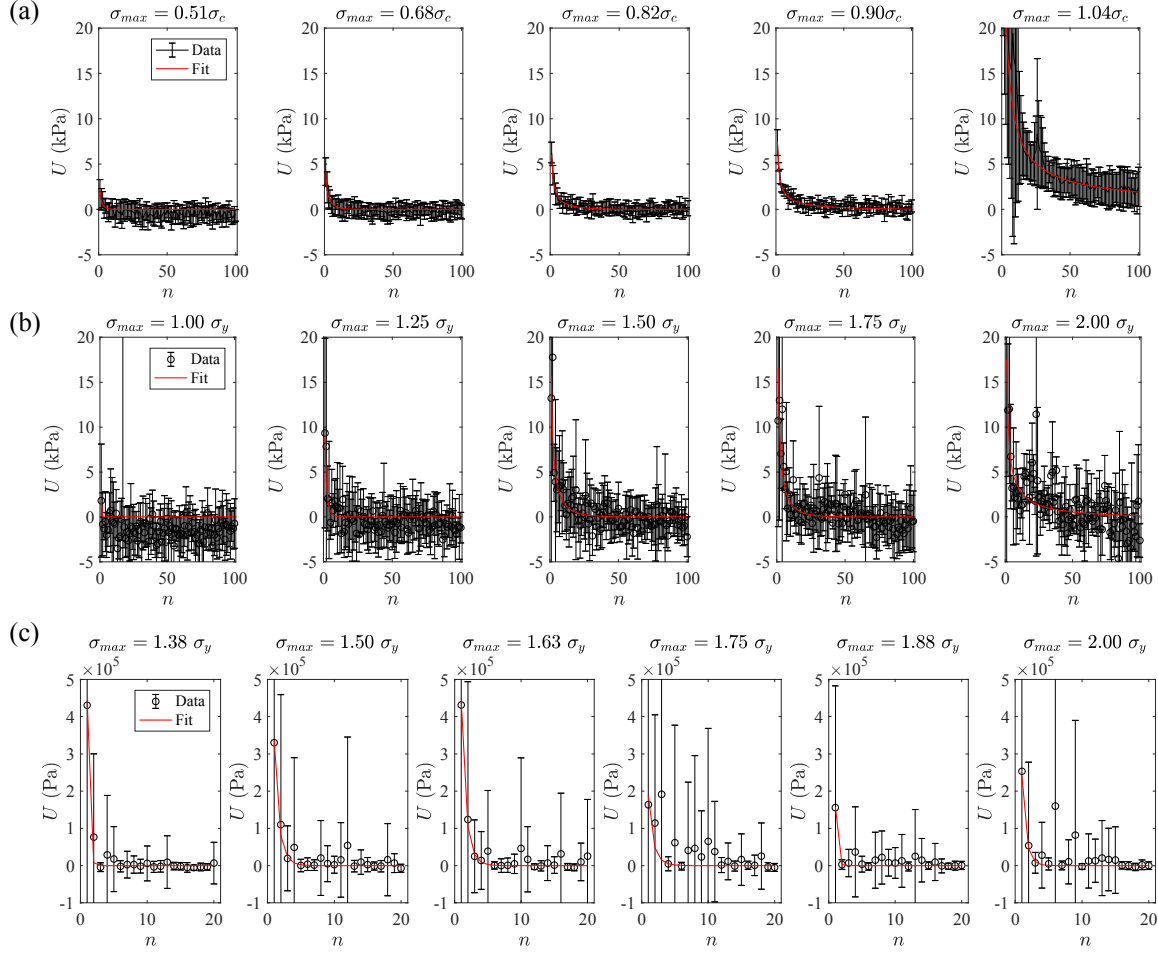


FIG. S15. **The precursor dissipation vs. number of cycle data for (a) 3 μm , (b) 1 μm , and (c) 500 nm diameter pillars.** For all sizes and in all steps with $\sigma_{\text{max}} < \sigma_c$, the precursor dissipation can be trained away after a certain number of cycles. The magnitude of precursor dissipation is in general larger in smaller size pillars. The initial precursor dissipation for (a) 3 μm , and (b) 1 μm pillars, grows as the maximum stress grows; the decay time also increases with stress. (c) There is no conclusive stress-dependent trend for the decay behavior of 500 nm pillars.

We examine and compare the cyclic precursor dissipation behavior between 500 nm, 1 μm and the 3 μm diameter pillars following the same fitting analysis procedures described in Sec. S5 but with $U_\infty = 0$. The data and fitting curves are shown in Fig. S15. It is worth noting that the training tests for 500 nm diameter pillars have too small unloading/reloading amplitude for drift correction. For all sizes of pillars, the precursor dissipation can be trained away after a certain number of cycles.

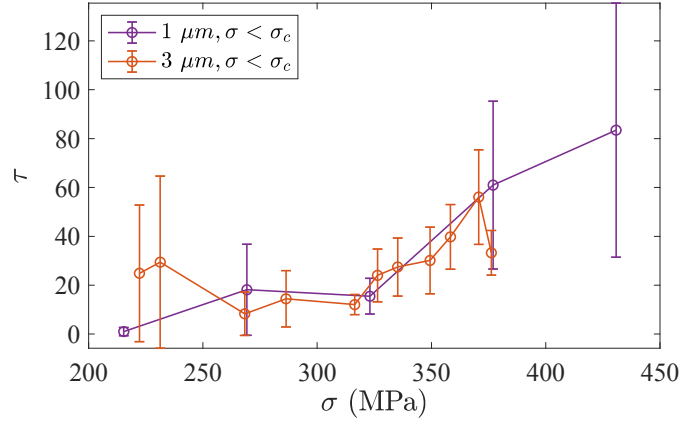


FIG. S16. **Characteristic decay time τ versus the maximum stress estimated for different pillar sizes** (1 μm vs. 3 μm diameter copper pillars).

For 1 μm diameter pillars, the initial precursor dissipation grows as the maximum stress grows; the decay time also increases with stress, as shown in Fig. S16 in comparison with the τ divergence behavior of 3 μm diameter pillars. In this comparison, the stress is not normalized because a quasi-static measurement for the critical stress is not accessible – the smaller pillars cannot be loaded to σ_c before the large plastic deformation collapses their compression geometry. For 500 nm diameter pillars, we can hardly distinguish the training behaviors at different maximum stress from the available data.

REFERENCES

1. X. Ni, S. Papanikolaou, G. Vajente, R. X. Adhikari, and J. R. Greer, *Phys. Rev. Lett.* **118**, 155501 (2017).
2. R. Maass, M. Wraith, J. T. Uhl, J. R. Greer, and K. A. Dahmen, *Phys. Rev. E* **91**, 042403 (2015).
3. I. N. Sneddon, *Int. J. Eng. Sci.* **3**, 47 (1965).
4. R. Cleveland and A. Ghosh, *Int. J. Plast.* **18**, 769 (2002).
5. F.F. Csikor, C. Motz, D. Weygand, M. Zaiser, and S. Zapperi, *Science* **318**, 251 (2007).
6. M. D. Uchic, P. A. Shade, and D. M. Dimiduk, *Annu. Rev. Mater. Res.* **39**, 361 (2009).
7. Y. Cui, Z. Liu, and Z. Zhuang, *Int. J. Plast.* **69**, 54 (2015).
8. A. T. Jennings, J. Li, and J. R. Greer, *Acta Mater.* **59**, 5627 (2011).
9. P. K. Agnihotri and E. Van Der Giessen, *Mech. Mater.* **90**, 37 (2015).
10. Y. Xiang and J. Vlassak, *Acta Mater.* **54**, 5449 (2006).
11. L. Nicola, Y. Xiang, J. J. Vlassak, E. Van der Giessen, and A. Needleman, *J. Mech. Phys. Solids* **54**, 2089 (2006).
12. J. Weiss, W.B. Rhouma, T. Richeton, S. Dechanel, F. Louchet, and L. Truskinovsky, *Phys. Rev. Lett.* **114**, 105504 (2015).
13. L. Corté, P. M. Chaikin, J. P. Gollub, and D. J. Pine, *Nat. Phys.* **4**, 420 (2008).

14. D. W. Marquardt, *J. Soc. Ind. Appl. Math.* **11**, 431 (1963).
15. W. Press, B. Flannery, S. Teukolsky, and W. Vetterling, *Numerical Recipes* (Cambridge University Press, Cambridge, England, 1986), pp. 430–436.
16. M. M. Bandi, H. G. E. Hentschel, I. Procaccia, S. Roy, and J. Zylberg, *Europhys. Lett.* **122**, 38003 (2018).